Refractive-index-sensing optical comb based on photonic radio-frequency conversion with intracavity multi-mode interference fiber sensor

RYO OE,[1,2,9] **SHUJI TAUE,**[3,4,9] **TAKEO MINAMIKAWA,**[2,5] **KOSUKE NAGAI,**[1] **KYUKI SHIBUYA,**[1,2] **TAKAHIKO MIZUNO,**[2,5] **MASATOMO YAMAGIWA,**[2,5] **YASUHIRO MIZUTANI,**[2,6] **HIROTSUGU YAMAMOTO,**[2,7] **TETSUO IWATA,**[2,5] **HIDEKI FUKANO,**[3] **YOSHIAKI NAKAJIMA,**[2,8] **KAORU MINOSHIMA,**[2,8] **AND TAKESHI YASUI**[2,5,*]

[1]*Graduate School of Advanced Technology and Science, Tokushima University, 2-1, Minami-Josanjima, Tokushima, Tokushima 770-8506, Japan*
[2]*JST, ERATO, MINOSHIMA Intelligent Optical Synthesizer Project, 2-1, Minami-Josanjima, Tokushima, Tokushima 770-8506, Japan*
[3]*Graduate School of Natural Science and Technology, Okayama University, 3-1-1 Tsushima-naka, Kita-ku, Okayama, Okayama 700-8530, Japan*
[4]*School of System Engineering, Kochi University of Technology, 185 Miyanokuchi, Tosayamada, Kami, Kochi 782-8502, Japan*
[5]*Graduate School of Technology, Industrial and Social Sciences, Tokushima University, 2-1, Minami-Josanjima, Tokushima, Tokushima 770-8506, Japan*
[6]*Graduate School of Engineering, Osaka University, 2-1, Yamadaoka, Suita, Osaka 565-0871, Japan*
[7]*Center for Optical Research and Education, Utsunomiya University, 7-1-2, Yoto, Utsunomiya, Tochigi 321-8585, Japan*
[8]*Graduate School of Informatics and Engineering, The University of Electro-Communications, 1-5-1, Japan*
[9]*These authors contributed equally to this work*
*yasui.takeshi@tokushima-u.ac.jp

Abstract: Optical frequency combs (OFCs) have attracted attention as optical frequency rulers due to their tooth-like discrete spectra together with their inherent mode-locking nature and phase-locking control to a frequency standard. Based on this concept, their applications until now have been demonstrated in the fields of optical frequency metrology. However, if the utility of OFCs can be further expanded beyond their application by exploiting new aspects of OFCs, this will lead to new developments in optical metrology and instrumentation. Here, we report a fiber sensing application of OFCs based on a coherent link between the optical and radio frequencies, enabling high-precision refractive index measurement based on frequency measurement in radio-frequency (RF) region. Our technique encodes a refractive index change of a liquid sample into a repetition frequency of OFC by a combination of an intracavity multi-mode-interference fiber sensor and wavelength dispersion of a cavity fiber. Then, the change in refractive index is read out by measuring the repetition frequency in RF region based on a frequency standard. Use of an OFC as a photonic RF converter will lead to the development of new applications in high-precision fiber sensing with the help of functional fiber sensors and precise RF measurement.

1. Introduction

An optical frequency comb (OFC) [1–3] is regarded as a group of a vast number of phase-locked narrow-linewidth continuous-wave (CW) light sources with a constant frequency spacing f_{rep} (typically, 50–100 MHz) over a broad spectral range. The inherent mode-locking nature and active laser control enable us to use an OFC as an optical frequency ruler traceable

to a microwave or radio-frequency (RF) frequency standard. Based on the concept of an optical frequency ruler, OFCs have found many applications in optical frequency metrology and distance metrology; examples include atomic spectroscopy [2], gas spectroscopy [4], solid spectroscopy [5], spectroscopic ellipsometry [6], strain sensing [7], and distance measurement [8]. Also, time characteristics of OFC has been applied for the ultrafast spectroscopy by the help of asynchronous optical sampling [9,10]; for example, detection of coherent phenomena [11,12] and relaxation dynamics of saturable absorber [13]. If the application fields of OFCs could be expanded beyond those previous application, the adoption of OFCs as next-generation lasers will grow in optical metrology and instrumentation.

One interesting feature of OFCs is a coherent link between the optical and radio frequencies. For example, when an OFC is detected with a photodiode, its quadratic-detection function converts a mode spacing of OFC into a beat signal in the RF region without changing f_{rep}. While the mode spacing of the OFC is transferred into the RF beat signal via such a coherent detection process, use of the RF beat signal simplifies the experimental methodology because measurement in the RF region benefits from high precision, high functionality, convenience, and low cost by making use of various kinds of RF measurement apparatuses. Therefore, the RF beat signal and its harmonic components have been applied to optical distance metrology, such as long-distance measurement with extremely high precision [14–16].

The key feature required to enable this new use of OFC is a photonic RF conversion function in a fiber OFC cavity. The repetition frequency f_{rep} in a ring cavity is given by

$$f_{rep} = \frac{c}{nL},\tag{1}$$

where c is the speed of light in vacuum, n is the group refractive index of the cavity fiber, and L is the geometrical length of the fiber cavity. If an external disturbance, such as a temperature change, strain, or vibration, interacts with the fiber OFC cavity, f_{rep} shifts as a result of a change of the optical cavity length nL. In other words, the OFC can act as a photonic RF converter for such an external disturbance. Since RF frequency measurement can be performed with high precision and a wide dynamic range by making use of accurate frequency standards, the combination of a photonic RF converter and RF frequency measurement, namely, a photonic RF sensor, has the potential to greatly enhance the precision and dynamic range compared with those of conventional electrical or photonic sensors. Although this use of a photonic RF sensor has been demonstrated for strain [17], strain/temperature [18,19], and ultrasound [20,21] by use of multiple-longitudinal-mode or multiple-polarization-mode spacing in a CW fiber laser, use of an OFC will further benefit from the ultra-narrow linewidth and high stability of f_{rep} due to the inherent nature of the mode-locking oscillation. However, when a cavity single-mode fiber (SMF) itself is used as a sensor, the measurable sensing quantities are limited to physical quantities that directly interact with the fiber OFC cavity, such as strain [22], acoustic pressure [23], or ultrasound waves [24].

Photonic RF sensors that can sense a wide variety of physical quantities will become possible if a functional fiber sensor can be introduced into a fiber OFC cavity. Such intracavity fiber sensors will benefit from the sensitivity enhancement made possible by the multiple passages of light through the sensor in addition to photonic RF conversion. One interesting application of photonic RF sensors is in sensing of refractive index (RI) because fiber RI sensors have found many applications in ethanol sensing [25], glucose sensing [26], bio-sensing [27], and gas sensing [28]. In these applications, shift of optical spectrum or change of optical intensity has been measured. However, the precision of RI sensing is limited by the instrument performance; these applications still need even greater sensing

performance. If high-precision RF measurement can be used for the optical RI sensing, its sensing precision will be largely enhanced.

In this article, we focus on a multi-mode interference (MMI) fiber sensor for RI measurement [29–31]. An MMI fiber sensor is composed of a clad-less multi-mode fiber (MMF) with a pair of SMFs at the two ends, has good compatibility with fiber OFC cavities, and works as an RI sensor based on a change in MMI wavelength λ_{MMI} due to the Goos-Hänchen shift on the surface of the clad-less MMF [Fig. 1(a), see Materials and methods]. An RI-dependent shift of λ_{MMI} in the fiber OFC cavity is converted into a shift of f_{rep} via wavelength dispersion of the cavity fiber [Fig. 1(b)]. In our setup, we introduced an MMI fiber sensor into a fiber OFC cavity, forming what we call an MMI-OFC, and read out the change in RI in a sample solution via f_{rep} to demonstrate the potential of MMI-OFCs as photonic RF sensors for RI.
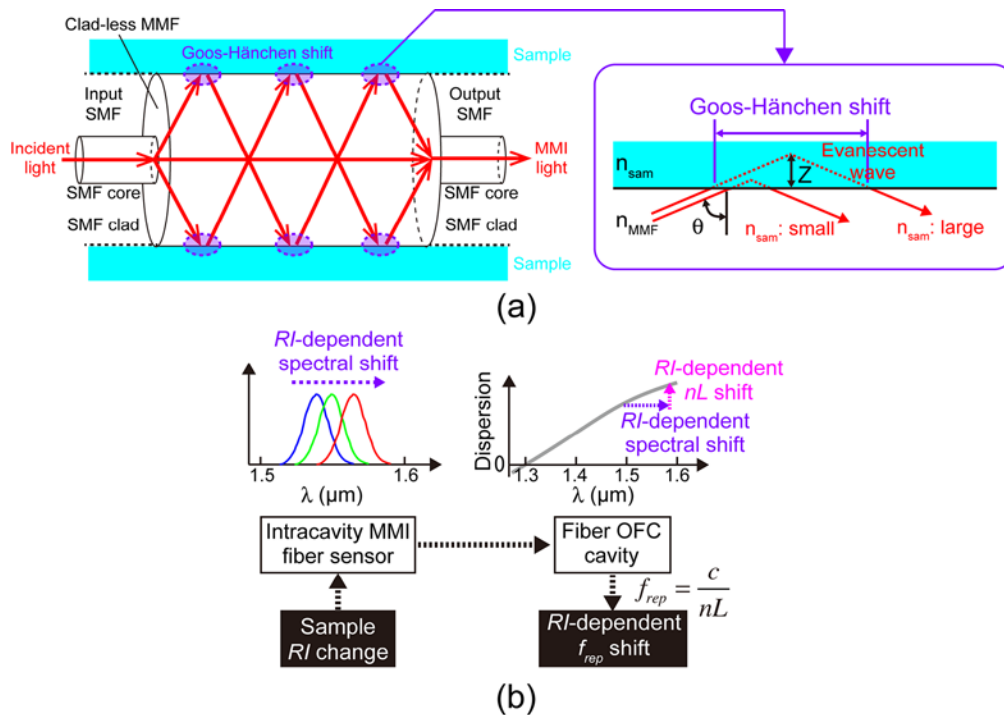

Fig. 1. Principle of operation. (a) Schematic diagram of the MMI fiber sensor. An inset of Fig. 1(a) shows a schematic drawing of the Goos-Hänchen shift on the surface of the clad-less MMF. The MMI fiber sensor functions as an RI-dependent tunable bandpass filter via the MMI process. (b) Conversion from sample RI change to RI-dependent f_{rep} shift. The intracavity MMI fiber sensor shifts the optical spectrum of the MMI-OFC depending on the sample RI. The wavelength-shifted MMI-OFC spectrum experiences the wavelength dispersion of the cavity fiber, resulting in the conversion from an RI-dependent spectral shift to an RI-dependent shift of the optical cavity length nL. Such an RI-dependent nL shift leads to an RI-dependent f_{rep} shift based on Eq. (1).

2. Materials and methods

2.1 MMI fiber sensor

A schematic diagram of the MMI fiber sensor is shown in Fig. 1(a). Broadband light passing through the input SMF is diffracted at the entrance face of the clad-less MMF, and then repeats total internal reflection at the boundary between the clad-less MMF surface and the sample solution (typical number of reflections: a few tens to a few hundreds). When a light beam undergoes total internal reflection in the clad-less MMF, the beam is spatially shifted as

if it had briefly penetrated the surface before bouncing back (Goos-Hänchen shift), as shown in an inset of Fig. 1(a). The penetration Z is given by [32]

$$Z = \frac{\lambda/n_{MMF}}{2\pi\sqrt{\sin^2\theta - \left(n_{sam}/n_{MMF}\right)^2}}, \tag{2}$$

where λ is the wavelength of transmitting light, n_{MMF} is the refractive index of the clad-less MMF, θ is the incident angle of the light to the cladding, and n_{sam} is the sample RI. When the order of the MMI, m, is equal to 4, all modes of light are refocused as shown in Fig. 1(a), and the constructive interference of light has the maximum peak intensity at the MMI wavelength λ_{MMI} [32]. λ_{MMI} light mainly exits through the clad-less MMF and then goes toward the output SMF. λ_{MMI} is given by [33]

$$\lambda_{MMI} = \frac{n_{MMF}m}{L_{MMF}}[D(n_{scan})]^2, \tag{3}$$

where L_{MMF} is the geometrical length of the clad-less MMF and $D(n_{sam})$ is the effective diameter of the clad-less MMF influenced by the Goos-Hänchen shift [see an inset of Fig. 1(a)]. From Eqs. (2) and (3), when n_{sam} changes, Z and the corresponding $D(n_{sam})$ change; therefore, λ_{MMI} becomes a function of n_{sam}. Since the intracavity MMI fiber sensor also receives the similar effect, the MMI-OFC output light shows the RI-dependent shift of optical spectrum. Such RI-dependent optical-spectrum shift experiences the wavelength dispersion of the cavity fiber rather than the intracavity MMI fiber sensor. In other words, the change of nL in Eq. (1), caused by the RI-dependent optical-spectrum shift, leads to the RI-dependent f_{rep} shift. Within the limited range of the sample RI, this RI-dependent f_{rep} shift can be linearized as demonstrated later.

The MMI fiber sensor was composed of a clad-less MMF (core diameter = 125 µm, fiber length = 58 mm) with a pair of SMFs at both ends (core diameter = 6 µm, clad diameter = 125 µm, fiber length = 54 mm), in which the diameter of the SMF clad was equal to that of the clad-less MMF core. In the present MMI-OFC, we set m to 4 for use of the intracavity MMI fiber sensor as the RI-dependent tunable band-pass filter. Due to the spectral bandpass-filtering effect in the MMI process, the MMI fiber sensor acts as an RI sensor showing an RI-dependent λ_{MMI} shift. We designed the parameters of the MMI fiber sensor so that the spectral peak appeared around the center wavelength of fiber OFC (= 1555 nm) when the sample is a pure water sample (0 EtOH%, RI = 1.333 refractive index units or RIU).

2.2 Experimental setup

We used a mode-locked Er:fiber laser oscillator for the MMI-OFC (see Fig. 2). This oscillator had a ring cavity including a 2.9 m length of single-mode fiber (SMF, SMF-28, Corning, dispersion at 1550 nm = 17 ps/km/nm), a 1.6 m length of erbium-doped fiber (EDF, ER30-4/125, LIEKKI, dispersion at 1550 nm = −15 ps/km/nm), a polarization controller [PC, PCUA-15-S/F(15P/15Q/15H), Optoquest Co., Ltd.], a polarization-insensitive isolator (ISO, PSSI-55-P-I-N-B-I, AFR), a 70:30 fiber coupler (FC, SBC-1-55-30-1-B-1, AFR), a wavelength-division-multiplexing coupler (WDM, WDM-1-9855-1-L-1-F, AFR), and a pumping laser diode (LD, BL976-PAG900, Thorlabs, wavelength = 980 nm, power = 900 mW). The temperature of the fiber cavity was controlled to 25.0°C by a combination of a Peltier heater (TEC1-12708, Kaito Denshi, power = 76 W), a thermistor (PB7-42H-K1, Yamaki), and a temperature controller (TED200, Thorlabs, PID control). Stable soliton mode-locking oscillation was achieved by nonlinear polarization rotation with near zero cavity dispersion (= −0.045 pm/s²) before and after introducing the MMI fiber sensor in the cavity. The output light from the oscillator was detected by a photodetector (PD), and its f_{rep} was

measured by an RF frequency counter (53230A, Keysight Technologies, frequency resolution = 12 digit/s) and an RF spectrum analyzer (E4402B, Keysight Technologies, frequency resolution = 1 Hz), both of which were synchronized to a rubidium frequency standard (FS725, Stanford Research Systems, accuracy = 5×10^{-11} and instability = 2×10^{-11} at 1 s). Also, its optical spectrum was measured by an optical spectrum analyzer (AQ6315A, Yokogawa Electric Corp., wavelength accuracy = 0.05 nm, wavelength resolution = 0.05 nm).

2.3 Samples

Mixtures of ethanol and pure water were used as standard samples. The sample RI was adjusted by changing the mixture ratio between ethanol and water. The relationship between the ethanol concentration EC (unit: EtOH%) and the sample RI (unit: RIU) is given by [34]

$$RI = 1.3326 + 4.90 \times 10^{-4} \times EC. \qquad (4)$$

The temperature of the sample was controlled to 22°C by a combination of a K-type thermocouple (TJA-550K, AS ONE), a cord heater (603-60-69-01, Tokyo Glass Kikai, power = 15 W), and a temperature controller (TJA-550, AS ONE, PID control, display resolution = 0.1°C).
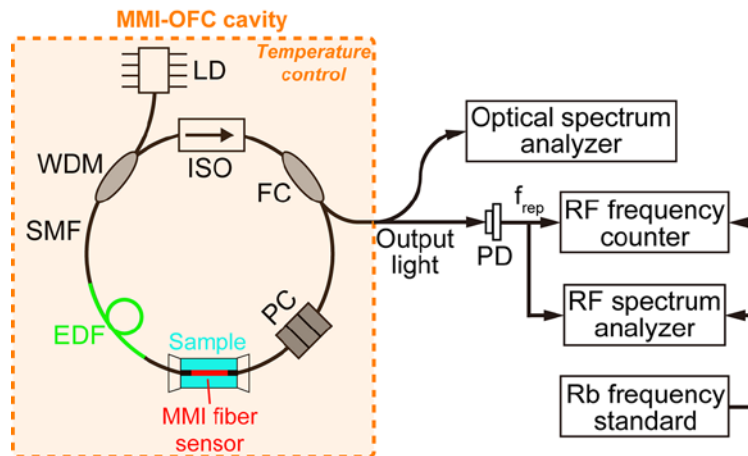

Fig. 2. Experimental setup. See Materials and methods for details.

3. Results

3.1 Basic characteristics of fiber OFC

Stable mode-locking oscillation in the MMI-OFC is indispensable for high-precision RI sensing. Here we compare an optical spectrum of the MMI-OFC with that of a usual OFC. The blue line in Fig. 3 shows an optical spectrum of a usual OFC (center wavelength = 1561.8 nm, spectral bandwidth = 15 nm, mean power = 4.7 mW), indicating the symmetrical broad spectrum, together with some spikes due to the soliton mode-locking oscillation near the zero-dispersion region of the cavity (-0.045 pm/s^2). On the other hand, the red line in Fig. 3 shows an optical spectrum of an MMI-OFC. The spectral bandpass-filtering effect of the intracavity MMI fiber sensor decreased the spectral bandwidth and the mean power to 10 nm and 2.9 mW, respectively. In this way, we could obtain stable mode-locking oscillation even in the MMI-OFC.
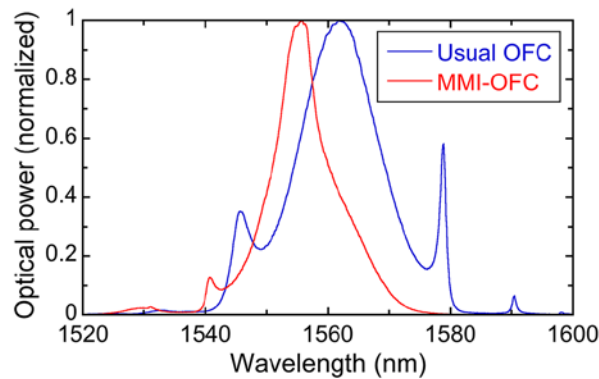
Fig. 3. Comparison of optical spectrum between usual OFC and MMI-OFC.

Next, we investigate RF spectra of the MMI-OFC light because the multi-mode propagation and polarization spread in the intracavity MMI fiber sensor may superimpose unnecessary parasitic side modes on the RF beat signal. Figure 4(a) shows the RF spectrum of the MMI-OFC light within the frequency range of 0 to 3000 MHz when the resolution bandwidth (RBW) and the video resolution bandwidth (VBW) were set to 300 kHz. The fundamental component and 68 harmonic components of repetition frequency appeared as frequency spikes with a constant frequency spacing of f_{rep}, namely RF com modes; however, no additional signals appear in gap regions between these modes. We next expanded the spectral region of the fundamental component ($= f_{rep} = 43.0176$ MHz) with different spectral range and RBW/VBW, as shown in Figs. 4(b), 4(c), and 4(d). Only single sharp spike was confirmed. We next expanded the spectral region of the 49-th harmonic component ($= 49f_{rep} = 2107.862$ MHz), as shown in Figs. 4(e), 4(f), and 4(g). Again, only the single sharp spike was confirmed. In this way, the intracavity MMI fiber sensor did not generate any parasitic side modes in the RF region.

It is also interesting to investigate the existence of such the parasitic side modes in the optical frequency region. To this end, we prepared a narrow-linewidth CW laser (PLANEX, Redfern Integrated Optics, Inc., center wavelength: 1,550 nm; FWHM: <2.0 kHz) and phase-locked it to a commercialized OFC (OCLS-HSC-D100-TKSM, Neoark Co., center wavelength = 1560 nm, spectral bandwidth = 20 nm, repetition frequency = 100 MHz, carrier-envelope-offset frequency = 10.5 MHz, phase-locked to the RF frequency standard). Linewidth of the phase-locked CW laser light is estimated to several kHz. Then, the phase-locked CW laser light was interfered with the output light of the MMI-OFC by a fiber coupler (not shown in Fig. 2). Figure 5 shows the RF spectrum of the optical beat signal between the CW laser light and the MMI-OFC light. In addition to the f_{rep} signal, the beat signal (freq. = f_{beat}) between the CW laser light and the most adjacent MMI-OFC mode and its mirror signal (freq. = $f_{rep} - f_{beat}$) were clearly confirmed. Due to no active stabilization of the repetition frequency and the carrier-envelope-offset frequency in the MMI-OFC, the f_{beat} signal fluctuated with the somewhat broader linewidth (see Visualization 1); however, no parasitic side modes appear in the optical frequency region.
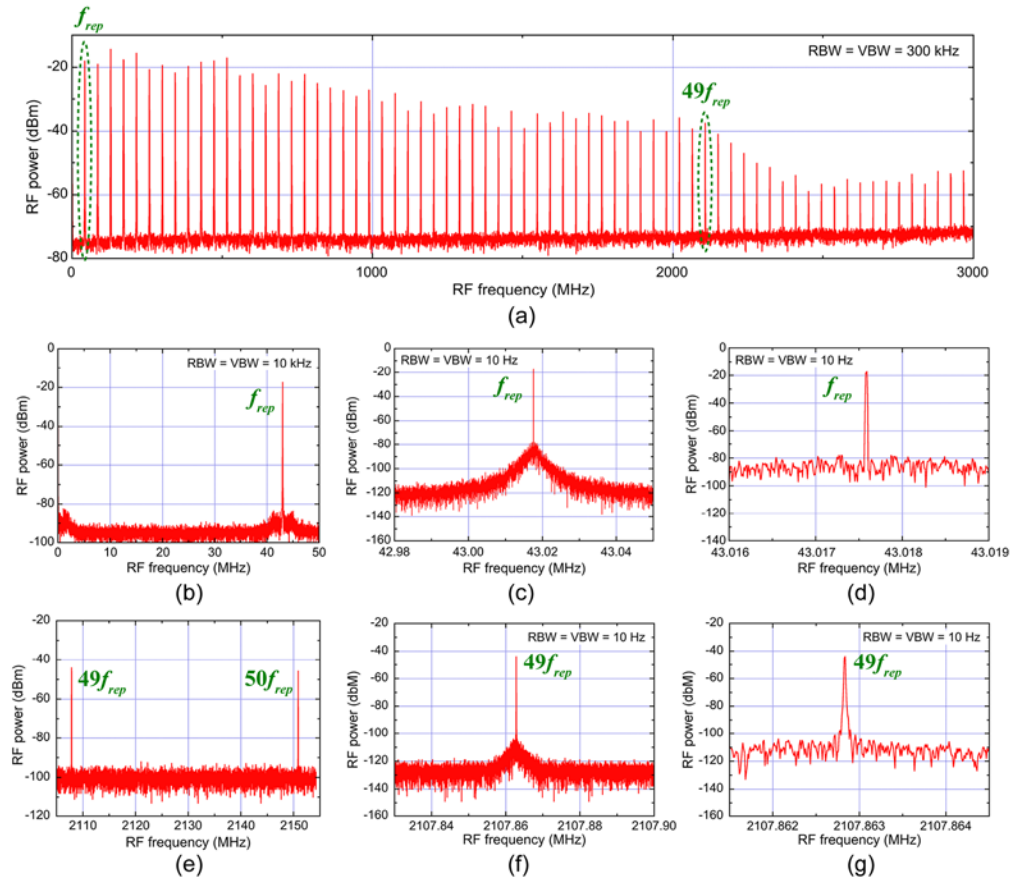
Fig. 4. (a) RF spectrum of the RF comb mode within the frequency range of 3000 MHz. RF spectrum of the fundamental component with the frequency range of (b) 50 MHz, (c) 0.07 MHz, and (d) 0.003 MHz. RF spectrum of the 49-th harmonic component with the frequency range of (b) 50 MHz, (c) 0.07 MHz, and (d) 0.003 MHz RBW, resolution bandwidth; VBW, video bandwidth.
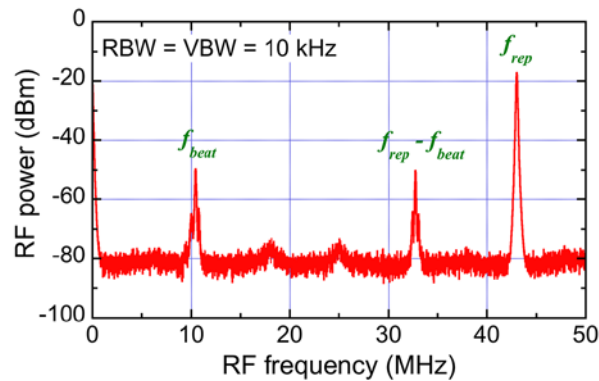

Fig. 5. RF spectrum of the optical beat signal between one mode of the MMI-OFC and a CW laser light phase-locked to another fully stabilized OFC (see Visualization 1).

We further compare the fluctuation of f_{rep} between the MMI-OFC and the usual OFC. f_{rep} in the MMI-OFC was 43.19 MHz, whereas that in the usual OFC was 43.06 MHz. Fig. 6 shows a comparison of the fluctuation in f_{rep} between the usual OFC (blue plots) and the

MMI-OFC (red plots) with respect to gate time. The fluctuation in f_{rep} is indicated by the Allan deviation. The fluctuation in f_{rep} showed similar behavior in the usual OFC and the MMI-OFC: the fluctuation decreased at gate times below 0.2 s, whereas it increased at gate times over 0.2 s. The drift behavior of f_{rep} still remained even at gate times greater than 0.2 s, although the temperature of the OFC cavity was stabilized; this behavior is typical in f_{rep}-unstabilized OFCs [35]. The f_{rep} fluctuation in the MMI-OFC reached a minimum value of 0.0302 Hz at a gate time of 0.2 s. Most importantly, the introduction of the MMI fiber sensor into the fiber OFC cavity had little effect on the fluctuation in f_{rep}, enabling us to perform high-precision RI sensing based on the stable f_{rep}.
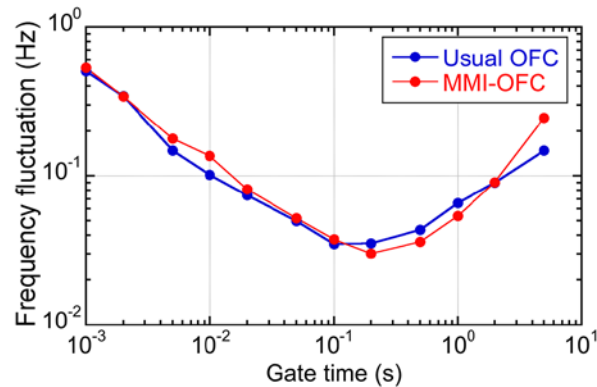

Fig. 6. Comparison of frequency fluctuation between usual OFC and MMI-OFC.

3.2 RI-dependent shift of optical spectrum

Next, we investigated the shift of the optical spectrum with respect to the sample RI. Ethanol/water solutions with different mixture ratios (= 0–15 EtOH%, corresponding to 1.333–1.340 RIU) were used as samples with different RIs. We repeated the same experiment for 5 sets of ethanol/water samples with different RIs, and then calculated the mean and the standard deviation of them for each RI. Figure 7(a) shows a comparison of typical optical spectra of the ethanol/water samples with different RIs. Figure 7(b) shows the magnified spectrum of their peaks in Fig. 7(a). One can confirm the long-wavelength shift of the optical spectrum with increasing RI. Figure 7(c) show the relation between the sample RI and the shift of the center wavelength in the optical spectrum. The corresponding ethanol concentration is shown on the upper horizontal axis in Fig. 7(c). A positive linear relation between them was confirmed with a slope coefficient of 65.7 nm/RIU, indicated by a blue line. For comparison, we conducted a similar experiment using the ethanol/water solution sample (= 0–60 EtOH%, corresponding to 1.333–1.364 RIU) by placing the same MMI fiber sensor outside the cavity, namely the usual OFC and the extra-cavity MMI fiber sensor, to use the MMI fiber sensor in the usual way. The resulting slope coefficient was 53.5 nm/RIU as shown in Fig. 7(d) although the experimental data somewhat deviated from the linear relation. Reasonable match of the slope coefficient between them indicates that the MMI fiber sensor can work as an RI sensor even inside the fiber OFC cavity, in the same manner as the extra-cavity MMI fiber sensor.
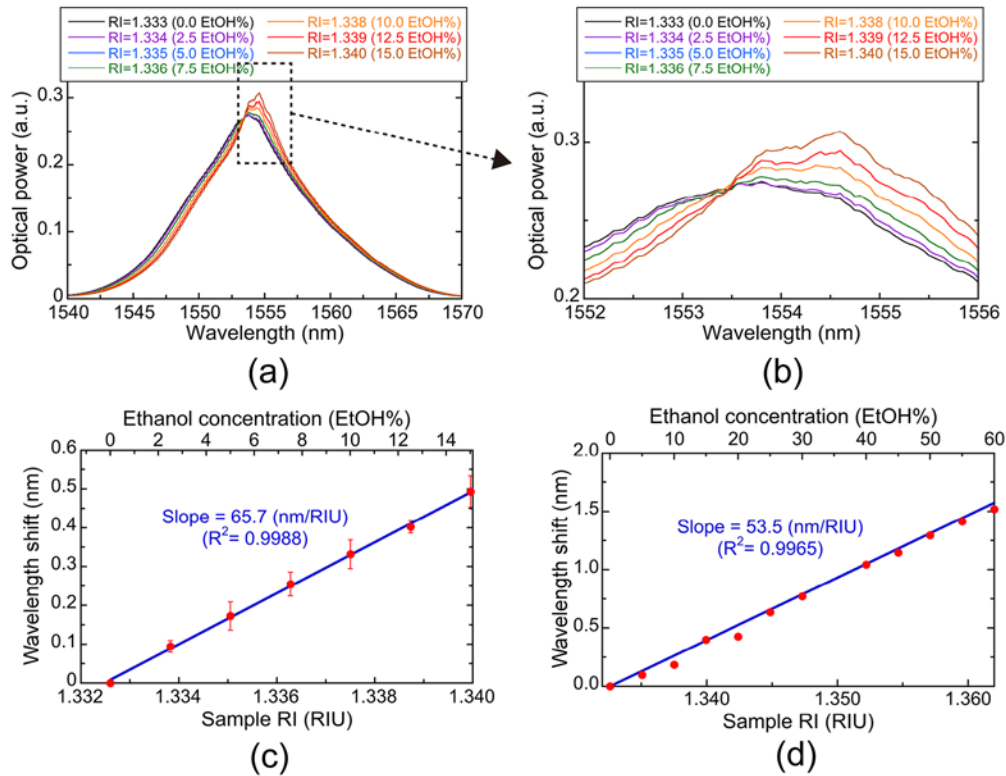
Fig. 7. RI-dependent shift of optical spectrum. (a) Optical spectra of MMI-OFC with respect to different sample RIs and (b) magnified spectra of their peaks. Increasing sample RI causes a long-wavelength shift of the optical spectrum. (c) Relation between sample RI and wavelength shift $\Delta\lambda$ in the MMI-OFC. Plots and error bars indicate the mean and the standard deviation of $\Delta\lambda$ in 5 repetitive measurements. (d) Relation between sample RI and wavelength shift $\Delta\lambda$ in the extra-cavity MMI fiber sensor. Blue line shows a linear approximation by a curve fitting analysis.

3.3 RI sensing based on f_{rep} shift

Finally, we performed RI measurement of ethanol/water samples with different mixture ratios (= 0–15 EtOH%, corresponding to 1.333–1.340 RIU) based on a shift in f_{rep}. Figure 8(a) shows the RI-dependent shift of the RF spectrum for f_{rep}, acquired by an RF spectrum analyzer. The linewidth of the RF spectra was limited by the instrumentation resolution of the RF spectrum analyzer rather than the actual linewidth of the f_{rep} signal. Nevertheless, the amount of spectral shift was significantly larger than the spectral linewidth, compared with the RI-dependent shift of the optical spectrum in Figs. 7(a) and 7(b). Such a high ratio of the spectral shift to the spectral linewidth enables high-resolution RI sensing based on RF measurement. Next, we measured f_{rep} values for 5 sets of ethanol/water samples with different RIs by using an RF frequency counter, and then calculated the mean and the standard deviation of their frequency shift for each RI. Figure 8(b) shows the relation between the sample RI and the f_{rep} shift in the MMI-OFC, indicating a negative linear relation between them with a slope coefficient of -6.19×10^3 Hz/RIU. Considering the positive relation in Fig. 7(c) and the negative net dispersion of the cavity fiber in this wavelength band, this negative slope is valid. Since the f_{rep} fluctuation was 0.0302 Hz at a gate time of 0.2 s [see red plots in Fig. 6], the RI resolution was estimated to be 4.88×10^{-6} RIU. On the other hand, the RI accuracy was estimated to be 5.35×10^{-5} RIU when it was defined as the root mean square (RMS) between the experimental data and the linear approximation. The differences of the RI

resolution and accuracy are mainly due to the influence of the cavity and/or sample temperature, as discussed later.
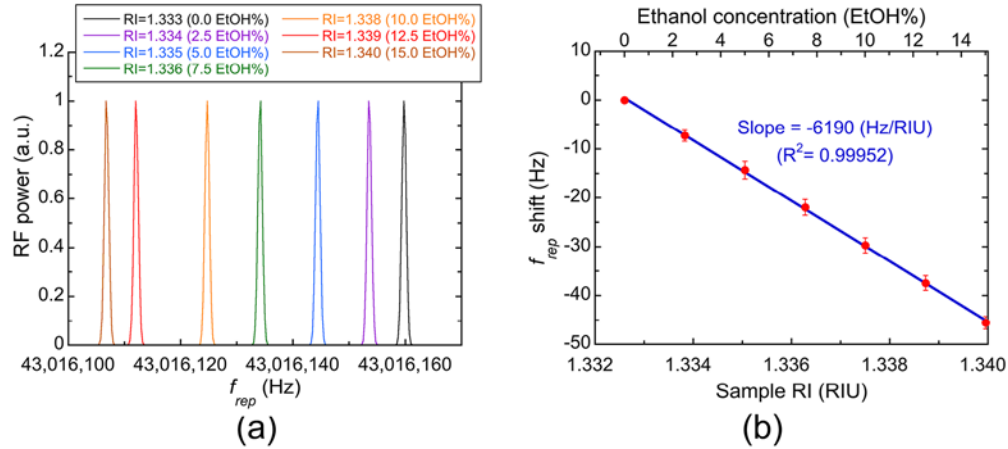

Fig. 8. RI-dependent f_{rep} shift. (a) RF spectra of f_{rep} signal with respect to different sample RI. Increasing sample RI causes decrease of f_{rep}. (b) Relation between sample RI and f_{rep} shift. Plots and error bars indicate the mean and the standard deviation of f_{rep} in 5 repetitive measurements. Blue line shows a linear approximation by a curve fitting analysis.

4. Discussion

We first discuss the validity of the RI-dependent f_{rep} shift [Fig. 8(b)]. An RI-dependent optical spectrum shift is converted into an RI-dependent f_{rep} shift via the wavelength dispersion of the cavity fiber [see Fig. 1(b)]. The present MMI-OFC cavity includes a 2.9-meter SMF with anomalous dispersion (= 17 ps/km/nm) and a 1.6-meter EDF with normal dispersion (= −15 ps/km/nm), leading to a net dispersion of 0.0253 ps/nm. From this net dispersion and the slope coefficient of 65.7 nm/RIU in Fig. 7(c), the relation between the time delay and sample RI is given as 1.66 ps/RIU, corresponding to −3.1 × 10^3 Hz/RIU. This estimated slope is in reasonable agreement with the experimental plots for the MMI-OFC [= −6.19 × 10^3 Hz/RIU, see Fig. 8(b)]. There are two reasons for the difference between the experimental slope and the estimated one: one is the change in the optical cavity length caused by the Goos-Hänchen shift in the intracavity MMI fiber sensor; the other is the wavelength dispersion of the intracavity MMI fiber sensor. Even including such an influence, the MMI-OFC functions as a correct photonic RF converter for RI.

Next, we discuss the influence of temperature fluctuation in the MMI-OFC cavity because such temperature fluctuation results in thermal expansion or shrinkage of the optical cavity length and hence leads to a change in nL and f_{rep}. We measured f_{rep} shift in the MMI-OFC with a pure water sample (= 0 EtOH%, RI = 1.333 RIU) when the cavity temperature T_{cav} was changed within the range of 20.0 to 21.4°C. Figure 9(a) shows the relation between the cavity temperature and f_{rep} shift. A linear relation was confirmed between them, and its slope was determined to be −177 Hz/°C by a linear approximation. On the other hand, the f_{rep} fluctuation in Fig. 6 was 0.0302 Hz at a gate time of 0.2 s. Therefore, if the f_{rep} fluctuation is mainly due to the fluctuation of T_{cav}, T_{cav} is estimated to be stabilized within 1.7 × 10^{-4} °C during a time period of 0.2 s.

We also investigated the relation between the sample temperature T_{sam} and the f_{rep} shift because the sample RI depends on both EtOH% and temperature. To this end, we measured f_{rep} shift when changing T_{sam} of a pure water sample (= 0 EtOH%, RI = 1.333 RIU) within the range of 22.0°C to 25.0°C, as shown in Fig. 9(b). A linear dependence of f_{rep} shift on T_{sam} was confirmed again; however, the slope constant (= −30.9 Hz/°C) was 6-times smaller than that of T_{cav}. Therefore, T_{cav} control is more important than T_{sam} control for high-resolution RI

sensing. If the f_{rep} fluctuation is influenced by the fluctuation of T_{sam} rather than that of T_{cav}, T_{sam} is estimated to be stabilized within 9.7×10^{-4} °C during a time period of 0.2 s. T_{sam} may further influence the RI accuracy because the reproducibility of T_{sam} in repetitive measurements appears in the RI accuracy. From the RI accuracy of 5.35×10^{-5} RIU in Fig. 8(b), the reproducibility of T_{sam} is estimated to be within 0.01°C. This value is reasonable considering the performance of the temperature controller.

Finally, we have a more in-depth discussion of the proposed method. The benefit of the proposed method was the precise photonic-to-RF conversion of the OFC, which is highlighted by comparing Figs. 7(a) and 8(a). Combination of this function with high-precision RF measurement benefits the high-resolution RI sensing. The achieved RI resolution ($= 4.88 \times 10^{-6}$ RIU) is 10-times higher than that of the previous research [30]. On the other hand, the measurable range of the sample RI was remained within the range of $1.3326 \sim 1.3424$ RIU, corresponding to $0 \sim 20$ EtOH%, because of the difficulty of maintaining the nonlinear-polarization-rotation-based mode-locking oscillation in MMI-OFC. Also, such nonlinear-polarization-rotation-based mode-locking oscillation limits high reproducibility of f_{rep} due to several degrees of freedom in the MMI-OFC cavity, such as the intracavity polarization controller or the pump LD current. Use of the saturable-absorption-based mode-locking oscillation, in place of the nonlinear-polarization-rotation-based mode-locking oscillation, will overcome these limitations due to its robust mode-locking oscillation and less degrees of freedom in the cavity.
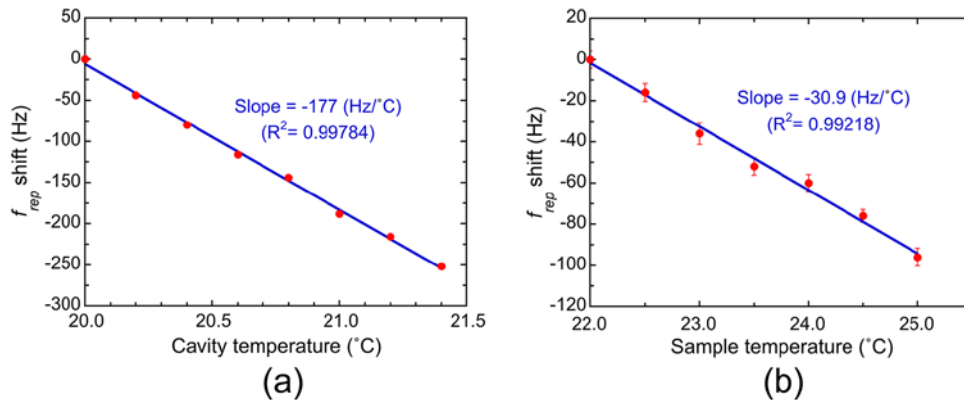

Fig. 9. Dependence of f_{rep} shift on temperature. (a) Cavity temperature dependence and (b) sample temperature dependence. Plots and error bars indicate the mean and the standard deviation of f_{rep} in 5 repetitive measurements. Blue line shows a linear approximation by a curve fitting analysis.

5. Conclusion

We integrated an MMI fiber sensor into a fiber OFC for f_{rep}-based RI measurement. The RI change of a liquid sample was transferred to a change in f_{rep} via multi-mode interference in the MMI fiber sensor and wavelength dispersion in the cavity fiber. Combined use of the MMI-OFC with high-precision RF measurement enables us to achieve an RI resolution of 4.88×10^{-6} RIU and an RI accuracy of 5.35×10^{-5} RIU. The concept of a precise photonic-RF-conversion OFC will expand the application scope of OFCs beyond their current use and will extend to fiber sensing, including RI sensing.

Funding

References

1. T. Udem, J. Reichert, R. Holzwarth, and T. W. Hänsch, "Accurate measurement of large optical frequency differences with a mode-locked laser," Opt. Lett. **24**(13), 881–883 (1999).
2. M. Niering, R. Holzwarth, J. Reichert, P. Pokasov, T. Udem, M. Weitz, T. W. Hänsch, P. Lemonde, G. Santarelli, M. Abgrall, P. Laurent, C. Salomon, and A. Clairon, "Measurement of the hydrogen 1S- 2S transition frequency by phase coherent comparison with a microwave cesium fountain clock," Phys. Rev. Lett. **84**(24), 5496–5499 (2000).
3. T. Udem, R. Holzwarth, and T. W. Hänsch, "Optical frequency metrology," Nature **416**(6877), 233–237 (2002).
4. S. A. Diddams, L. Hollberg, and V. Mbele, "Molecular fingerprinting with the resolved modes of a femtosecond laser frequency comb," Nature **445**(7128), 627–630 (2007).
5. A. Asahara, A. Nishiyama, S. Yoshida, K. I. Kondo, Y. Nakajima, and K. Minoshima, "Dual-comb spectroscopy for rapid characterization of complex optical properties of solids," Opt. Lett. **41**(21), 4971–4974 (2016).
6. T. Minamikawa, Y.-D. Hsieh, K. Shibuya, E. Hase, Y. Kaneoka, S. Okubo, H. Inaba, Y. Mizutani, H. Yamamoto, T. Iwata, and T. Yasui, "Dual-comb spectroscopic ellipsometry," Nat. Commun. **8**(1), 610 (2017).
7. N. Kuse, A. Ozawa, and Y. Kobayashi, "Static FBG strain sensor with high resolution and large dynamic range by dual-comb spectroscopy," Opt. Express **21**(9), 11141–11149 (2013).
8. I. Coddington, W. C. Swann, L. Nenadovic, and N. R. Newbury, "Rapid and precise absolute distance measurements at long range," Nat. Photonics **3**(6), 351–356 (2009).
9. P. A. Elzinga, R. J. Kneisler, F. E. Lytle, Y. Jiang, G. B. King, and N. M. Laurendeau, "Pump/probe method for fast analysis of visible spectral signatures utilizing asynchronous optical sampling," Appl. Opt. **26**(19), 4303–4309 (1987).
10. Y. Takagi and S. Adachi, "Subpicosecond optical sampling spectrometer using asynchronous tunable mode-locked lasers," Rev. Sci. Instrum. **70**(5), 2218–2224 (1999).
11. A. Bartels, R. Cerna, C. Kistner, A. Thoma, F. Hudert, C. Janke, and T. Dekorsy, "Ultrafast time-domain spectroscopy based on high-speed asynchronous optical sampling," Rev. Sci. Instrum. **78**(3), 035107 (2007).
12. A. Abbas, Y. Guillet, J.-M. Rampnoux, P. Rigail, E. Mottay, B. Audoin, and S. Dilhaire, "Picosecond time resolved opto-acoustic imaging with 48 MHz frequency resolution," Opt. Express **22**(7), 7831–7843 (2014).
13. A. Asahara and K. Minoshima, "Development of ultrafast time-resolved dual-comb spectroscopy," APL Photon. **2**(4), 041301 (2017).
14. K. Minoshima and H. Matsumoto, "High-accuracy measurement of 240-m distance in an optical tunnel by use of a compact femtosecond laser," Appl. Opt. **39**(30), 5512–5517 (2000).
15. K. Minoshima, K. Arai, and H. Inaba, "High-accuracy self-correction of refractive index of air using two-color interferometry of optical frequency combs," Opt. Express **19**(27), 26095–26105 (2011).
16. G. Wu, M. Takahashi, K. Arai, H. Inaba, and K. Minoshima, "Extremely high-accuracy correction of air refractive index using two-colour optical frequency combs," Sci. Rep. **3**(1), 1894 (2013).
17. S. Liu, Z. Yin, L. Zhang, L. Gao, X. Chen, and J. Cheng, "Multilongitudinal mode fiber laser for strain measurement," Opt. Lett. **35**(6), 835–837 (2010).
18. O. Hadeler, M. Ibsen, and M. N. Zervas, "Distributed-feedback fiber laser sensor for simultaneous strain and temperature measurements operating in the radio-frequency domain," Appl. Opt. **40**(19), 3169–3175 (2001).
19. O. Hadeler, E. Rønnekleiv, M. Ibsen, and R. I. Laming, "Polarimetric distributed feedback fiber laser sensor for simultaneous strain and temperature measurements," Appl. Opt. **38**(10), 1953–1958 (1999).
20. T. Guo, A. C. Wong, W. S. Liu, B. O. Guan, C. Lu, and H. Y. Tam, "Beat-frequency adjustable Er^{3+}-doped DBR fiber laser for ultrasound detection," Opt. Express **19**(3), 2485–2492 (2011).
21. Y. Liang, L. Jin, L. Wang, X. Bai, L. Cheng, and B.-O. Guan, "Fiber-laser-based ultrasound sensor for photoacoustic imaging," Sci. Rep. **7**(1), 40849 (2017).
22. T. Minamikawa, T. Ogura, Y. Nakajima, E. Hase, Y. Mizutani, H. Yamamoto, K. Minoshima, and T. Yasui, "Strain sensing based on strain to radio-frequency conversion of optical frequency comb," Opt. Express **26**(8), 9484–9491 (2018).
23. S. Wang, P. Lu, H. Liao, L. Zhang, D. Liu, and J. Zhang, "Passively mode-locked fiber laser sensor for acoustic pressure sensing," J. Mod. Opt. **60**(21), 1892–1897 (2013).
24. T. Minamikawa, T. Ogura, T. Masuoka, E. Hase, Y. Nakajima, Y. Yamaoka, K. Minoshima, and T. Yasui, "Optical-frequency-comb based ultrasound sensor," Proc. SPIE **10064**, 100645C (2017).
25. S. K. Srivastava, R. Verma, and B. D. Gupta, "Surface plasmon resonance based fiber optic sensor for the detection of low water content in ethanol," Sens. Actuators B Chem. **153**(1), 194–198 (2011).
26. S. Binu, V. P. Mahadevan Pillai, V. Pradeepkumar, B. B. Padhy, C. S. Joseph, and N. Chandrasekaran, "Fibre optic glucose sensor," Mater. Sci. Technol. C **29**(1), 183–186 (2009).
27. H. Tazawa, T. Kanie, and M. Katayama, "Fiber-optic coupler based refractive index sensor and its application to biosensing," Appl. Phys. Lett. **91**(11), 113901 (2007).
28. S. Sekimoto, H. Nakagawa, S. Okazaki, K. Fukuda, S. Asakura, T. Shigemori, and S. Takahashi, "A fiber-optic evanescent-wave hydrogen gas sensor using palladium-supported tungsten oxide," Sens. Actuators B Chem. **66**(1–3), 142–145 (2000).
29. Y. Jung, S. Kim, D. Lee, and K. Oh, "Compact three segmented multimode fibre modal interferometer for high sensitivity refractive-index measurement," Meas. Sci. Technol. **17**(5), 1129–1133 (2006).

30. Q. Wang and G. Farrell, "All-fiber multimode-interference-based refractometer sensor: proposal and design," Opt. Lett. **31**(3), 317–319 (2006).
31. S. Taue, Y. Matsumoto, H. Fukano, and K. Tsuruta, "Experimental analysis of optical fiber multimode interference structure and its application to refractive index measurement," Jpn. J. Appl. Phys. **51**(4S), 04DG14 (2012).
32. H. Fukano, D. Watanabe, and S. Taue, "Sensitivity characteristics of multimode-interference optical-fiber temperature-sensor with solid cladding material," IEEE Sens. J. **16**(24), 8921–8927 (2016).
33. J. E. Antonio-Lopez, A. Castillo-Guzman, D. A. May-Arrioja, R. Selvas-Aguilar, and P. Likamwa, "Tunable multimode-interference bandpass fiber filter," Opt. Lett. **35**(3), 324–326 (2010).
34. J. V. Herráez and R. Belda, "Refractive indices, densities and excess molar volumes of monoalcohols + water," J. Solution Chem. **35**(9), 1315–1328 (2006).
35. T. Yasui, R. Ichikawa, Y.-D. Hsieh, K. Hayashi, H. Cahyadi, F. Hindle, Y. Sakaguchi, T. Iwata, Y. Mizutani, H. Yamamoto, K. Minoshima, and H. Inaba, "Adaptive sampling dual terahertz comb spectroscopy using dual free-running femtosecond lasers," Sci. Rep. **5**(1), 10786 (2015).